DOI: 10.13009/EUCASS2017-13

On volumetric force distribution generated by dielectric barrier discharge actuator

S.L. Chernyshev, A.P. Kuryachii*, S.V. Manuilovich*, D.A. Rusyanov**
**Central Aerohydrodynamic Institute (TsAGI)*
1, Zhukovsky str., Zhukovsky, 140180 Moscow region, Russia

Abstract
Analytical expressions for spatial distribution of the time-averaged volumetric force generated by dielectric barrier discharge actuator are proposed in approximation of nondivergent field of this force. Calculated flow-field of the actuator induced near-wall jet agrees both qualitatively and quantitatively with experimental data. Main peculiarities of the distributions of the wall-normal and wall-parallel volumetric force components observed in experiments are explained.

1. Introduction

At present significant attention is given to study of possible applications of plasma actuators based on dielectric barrier discharge (DBD-actuators) for gas flow control. Detailed information concerning physical characteristics of plasma actuators and respective experimental studies can be finding in reviews [1-7]. Generated volumetric force and consumed electric power are the primary characteristics of DBD-actuators for many aerodynamic applications. These characteristics depend on a large number of geometric and physical parameters [5, 8] therefore an experimental optimization of DBD-actuator for any specific application is very labor-consuming. The problem of optimization of actuator parameters can be facilitated with the help of preliminary parametric numerical modelling with the use of adequate models of the volumetric force and heat release attainable in DBD-actuator. The efforts of many researchers to develop physico-mathematical models of DBD of high level complexity [9-14] up till now didn't result in any model convenient for routine numerical modelling. Therefore numerical simulations of flow-control based on DBD-actuator impact commonly use various simplified phenomenological models of volumetric force generated in DBD [15-21]. But namely experimental data concerning spatial distributions of the volumetric force have to help both in a clear understanding of physical mechanisms of the force production and in a development of adequate mathematical models by comparison results of numerical modelling with reliable experimental data [22].

Experimental estimations of two-dimensional distributions of the volumetric force generated by DBD-actuator commonly are based on particle image velocimetry (PIV) method permitting to measure with high accuracy both instantaneous and time-averaged flow fields induced by actuator [5]. The measured flow fields are used then to estimate the spatial distributions of the volumetric force components on the basis of two widely used methods. The first method is based on Navier-Stokes equations [23] and the second one uses the vorticity equation [24]. Different simplifying assumptions are applied in these methods. Nevertheless both methods result in similar distributions of the wall-parallel force component and identical values of the spatial integrated force [25, 26]. Based on these results, the conclusion on validity of simplifying assumptions accepted in both methods is drawn.

The spatial distribution of the wall-parallel force component obtained in experiments [25, 26] was approximated by analytic functions in [19]. The products of the second power polynomial and exponential function independently in wall-parallel and wall-normal directions were used. The dependent variables of this approximation has been adjusted using a least-squares fit to minimize the difference between experimental and calculated force distributions. Similar approach has been applied in [20] to approximate both wall-parallel and wall-normal force components. Numerical modelling after substitution of the analytic approximations of the force distributions in Reynolds-Averaged Navier-Stokes equations in [19] or compressible Navier-Stokes equations in [20] resulted in satisfactory agreement between calculated and measured flow fields. Note that the analytic approximations proposed in [19, 20] include 8 dependent variables in approximation of the wall-parallel force component and 64 variables in wall-normal component. In contrast to [19, 20], simple analytic expressions for spatial distributions of the volumetric force components qualitatively differing from distributions obtained in experiments[25, 26] by the methods [23, 24] have been proposed in [27]. Numerical modelling in the framework of Navier-Stokes equation with the use of the proposed force approximation permitted to explain the most of features of the experimental force distributions. Here other

DOI: 10.13009/EUCASS2017-13

simple analytic expressions for the force components are proposed and some peculiarity of the experimental force distribution is explained which was omitting in [27].

2. Peculiarities of experimental distributions of the volumetric force components

The experimental study of DBD-actuator executed in [25, 26] is simulated below. The design of actuator and the Cartesian coordinate system used in calculations are presented in upper Fig. 1. The DBD-actuator consists of two flat electrodes separated by a dielectric layer. The right edge of the upper exposed electrode is arranged under the left edge of the lower buried electrode. The buried electrode is grounded and the alternating high voltage is applied to the exposed electrode. The discharge ignites under the dielectric surface on the right from the exposed electrode. Dashed corves under the dielectric surface represent schematically the field lines of the time-averaged volumetric force arising in DBD.

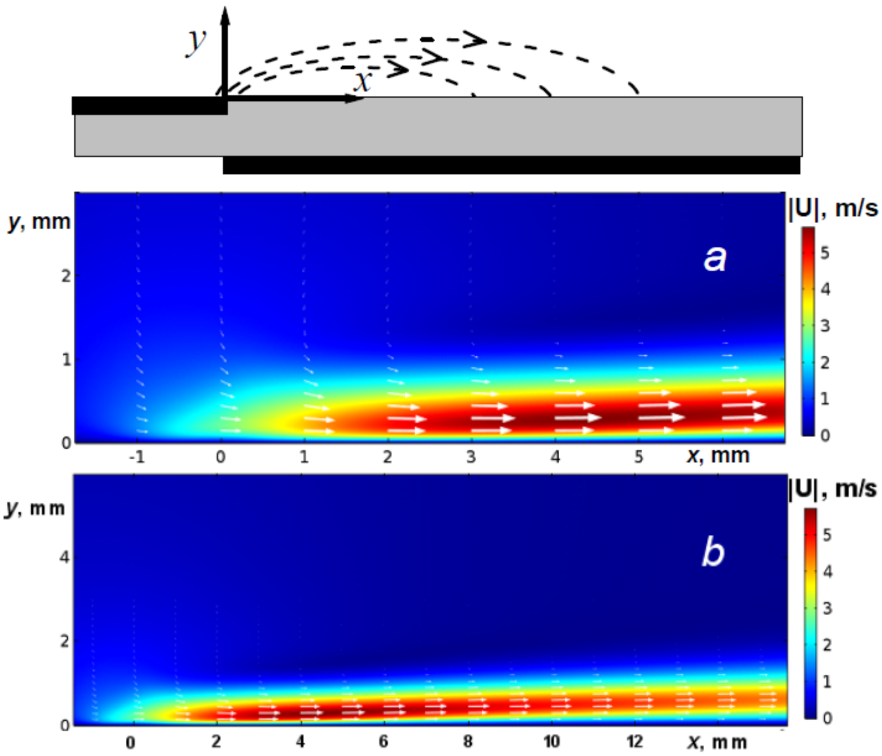

Figure 1: Design of DBD-actuator. Calculated velocity distributions of the induced near-wall jet

The mentioned above force-determination methods based on velocity field measurements [23, 24] imply two-dimensional, steady, incompressible flow. The method [23] (designated later as the method 1) relies on the momentum equations written for our convenience in the following form:

$$f_{x1}(x,y) \equiv f_x - \frac{\partial p}{\partial x} = \rho\left(u\frac{\partial u}{\partial x} + v\frac{\partial u}{\partial y}\right) - \mu\left(\frac{\partial^2 u}{\partial x^2} + \frac{\partial^2 u}{\partial y^2}\right), \quad (1)$$

$$f_{y1}(x,y) \equiv f_y - \frac{\partial p}{\partial y} = \rho\left(u\frac{\partial v}{\partial x} + v\frac{\partial v}{\partial y}\right) - \mu\left(\frac{\partial^2 v}{\partial x^2} + \frac{\partial^2 v}{\partial y^2}\right). \quad (2)$$

Here f_x and f_y are the volumetric force components along the appropriate axes, u and v are the velocity components, p is the static pressure, ρ and μ are the density and the dynamic viscosity of air. The subscript 1 denotes the force components estimated by the method 1.

All terms in the right sides of the equations (1), (2) are calculated using the measured time-averaged flow field and therefore are known. Unknown in experiment pressure field is excluded from a consideration due to neglecting the pressure gradient as compared with the volumetric force components:

DOI: 10.13009/EUCASS2017-13

$$\left|f_x\right| >> \left|\frac{\partial p}{\partial x}\right|, \quad \left|f_y\right| >> \left|\frac{\partial p}{\partial y}\right|. \tag{3}$$

Hence the method 1 estimates in fact the "seeming" force components including unknown pressure gradient.

The method [24] (designated as the method 2) excludes the unknown pressure distribution from a consideration by the use the vorticity equation which is obtained by differentiation of equations (1) and (2) on y and x, respectively, and subtraction the second resulting equation from the first one:

$$\frac{\partial f_x}{\partial y} - \frac{\partial f_y}{\partial x} = \rho\left(u\frac{\partial \omega}{\partial x} + v\frac{\partial \omega}{\partial y}\right) - \mu\left(\frac{\partial^2 \omega}{\partial x^2} + \frac{\partial^2 \omega}{\partial y^2}\right), \quad \omega = \frac{\partial v}{\partial x} - \frac{\partial u}{\partial y}. \tag{4}$$

Because in this case only one equation remains for two force components, it is assumed that the curl of the force is strongly dominated by vertical gradient of the wall-parallel force component, i.e.

$$\left|\frac{\partial f_x}{\partial y}\right| >> \left|\frac{\partial f_y}{\partial x}\right|. \tag{5}$$

Thus only the "seeming" wall-parallel force component f_{x2} is determined by the method 2 which is related with the real component f_x by the following expression:

$$f_{x2} \equiv f_x + \int_y^{\infty} \frac{\partial f_y}{\partial x}(x,s)\,ds = -\int_y^{\infty}\left[\rho\left(u\frac{\partial \omega}{\partial x} + v\frac{\partial \omega}{\partial y}\right) - \mu\left(\frac{\partial^2 \omega}{\partial x^2} + \frac{\partial^2 \omega}{\partial y^2}\right)\right] ds. \tag{6}$$

One can indicate the following intrinsic peculiarities of the distributions of the "seeming" force components f_{x1}, f_{y1}, and f_{x2} obtained in experiments [25, 26]. Note that these peculiarities are observed also in parametric experimental study [22] at variation both the amplitude and the frequency of the applied voltage.

1. The distributions of the wall-parallel force components f_{x1} and f_{x2} are qualitatively similar and contain the regions of elevated force located near the active edge of the exposed electrode (see Fig. 7 in [25]).

2. This region is more distinguished in the f_{x2} distribution.

3. The second local maximum of the wall-parallel force components f_{x1} and f_{x2} is observed downstream from the electrode edge at some distance from the dielectric surface.

4. Space integration of f_{x1} and f_{x2} results it the same values of the total wall-parallel force per unit length along the electrode edge.

5. The extremal value of the wall-normal force component f_{y1} is about the order of magnitude less than the maximum of the wall-parallel component f_{x1} (see Fig. 8, *a*, *b* in [26]).

6. The distribution of the wall-normal component f_{y1} contains the sign-alternating region near the edge of the exposed electrode (see Fig. 8, *b* in [26]).

7. The distributions of the wall-parallel force components f_{x1} and f_{x2} contain narrow near-wall regions of negative values arising at significant distance from the electrode edge (see Fig. 7 in [25]).

3. Analytic force distribution

The validity of the simplifying assumptions (3) and (5) has been revised in [28] where the approximation of a nondivergent nature of the volumetric force field [29] has been applied. The volumetric force in DBD is created mainly due to momentum transfer from ions accelerated by electric field to neutrals. Negative ions of oxygen participate in this procces when the potential of the exposed electrode decreases and positive ions of oxygen and nitrogen when the potential increases [30]. Ions of different sign and mass have different transport coefficients (mobility and diffusion) which though don't depend on electric field strength and, hence, on coordinates. Therefore one can consider that the volumetric force averaged during the cycle of the applied voltage is generated in unipolar charge medium with some average transport coefficients of charge carriers. The charge transfer in unipolar medium is governed by the following equation of charge conservation:

DOI: 10.13009/EUCASS2017-13

$$\frac{\partial q}{\partial t} + \nabla \cdot \mathbf{J} = S, \quad \mathbf{J} = q(b\mathbf{E} + \mathbf{V}) - D\nabla q. \tag{7}$$

Here q is the volumetric charge density, S is the algebraic sum of charge sources and sinks, $\mathbf{J}$, $\mathbf{E}$ and $\mathbf{V}$ are the vectors of the current density, the electric field strength, and the convective velocity of medium, b and D are the coefficients of mobility and diffusion of charge carriers.

For the steady-state case ($\partial/\partial t \equiv 0$) the algebraic sum of charge sources and sinks averaged during the applied voltage cycle equals zero. If the medium velocity $|\mathbf{V}| < 100$ m/s, the convective charge transfer can be neglected in comparison with the drift transfer, i.e. $|\mathbf{V}| << b|\mathbf{E}|$. Neglecting the diffusion transfer in the main region of the discharge yields the condition of nondivergent field of the volumetric force vector $\mathbf{f} = (f_x, f_y)$:

$$\nabla \cdot \mathbf{J} = b\nabla(q\mathbf{E}) = b\nabla\mathbf{f} = 0 \quad \text{or} \quad \frac{\partial f_x}{\partial x} + \frac{\partial f_y}{\partial y} = 0. \tag{8}$$

Simple model of the volumetric force satisfying the relation (8) based on only Gaussian functions for x and y coordinates has been considered in [28]. Here this model is modified with the aim to simulate the experiments [25, 26]. The analytic distributions of the force components denoted by the subscript 0 are specified as follows:

$$\begin{aligned} x \le x_m: \quad & f_{x0}(x,y) = A\left(1 + a\bar{x}^2\right)\exp\left(-\bar{x}^2\right)\exp\left(-\bar{y}^2\right), \\ & f_{y0}(x,y) = A\sqrt{\pi}\, y_0 \frac{\bar{x}(a-1) - a\bar{x}^3}{x_l}\exp\left(-\bar{x}^2\right)\mathrm{erfc}(\bar{y}), \quad \bar{x} = \frac{x - x_m}{x_l}, \end{aligned} \tag{9}$$

$$\begin{aligned} x > x_m: \quad & f_{x0}(x,y) = A\exp\left(-\bar{x}^2\right)\exp\left(-\bar{y}^2\right), \\ & f_{y0}(x,y) = -A\sqrt{\pi}\, y_0 \frac{\bar{x}}{x_r}\exp\left(-\bar{x}^2\right)\mathrm{erfc}(\bar{y}), \quad \bar{x} = \frac{x - x_m}{x_r}, \end{aligned} \tag{10}$$

$$\bar{y} = \frac{y}{y_0}, \quad a = 1 - \left(\frac{x_l}{x_r}\right)^2 \quad (x_l < x_r), \quad A = \frac{4F}{\pi\, y_0\left(x_l + x_r + 0.5ax_l\right)}, \quad \mathrm{erfc}(\bar{y}) = 1 - \frac{2}{\sqrt{\pi}}\int_0^{\bar{y}} \exp\left(-t^2\right)dt.$$

Here x_m is the coordinate of a maximum of the wall-parallel component f_{x0} achieving on the dielectric surface (the wall-normal component f_{y0} changes sign in this point), x_l and x_r are the characteristic scales of Gaussian distributions of the wall-parallel component at the left and at the right from the maximum, y_0 is the characteristic scale normal to the wall, F is the space integrated wall-parallel force per unit length along the exposed electrode edge. The formula (9) for f_{x0} contains the second power polynomial on x ensuring a continuity of the second derivative of f_{x0} on x what will be explained further.

The total wall-parallel force F depends on geometric and physical parameters of actuator and can be estimated, for example, with the help of empirical model [31]. Here the value $F = 0.025$ N/m is taken for a comparison with experiments [25, 26]. The following geometric parameters have been selected from the condition of a satisfactory agreement between calculated and experimental flow fields induced by actuator action: $x_m = 0.5$ mm, $x_l = 0.75$ mm, $x_r = 3$ mm, $y_0 = 0.9$·mm. The relation of characteristic scales $r = (x_l + x_r)/y_0 \approx 4$ seemingly is typical for the force distributions created by DBD-actuators.

Results of numerical modeling on the base of steady incompressible Navier-Stokes with the volumetric force determined by the equations (9)-(10) are presented on Fig. 1. Details of calculational procedure can be finding in [27]. The spatial distributions of the absolute of values of the velocity vector are shown on Fig. 1, *a*, *b* in different scales for comparison with experimental data presented on Fig. 5, *a*, *b* in [25]. This comparison demonstrates both qualitative and quantitative coincidence of the calculated flow field achieved by simple model of the volumetric force (9)-(10) containing only 5 parameters.

4. Explanation of peculiarities of the force distributions observed in experiments

The spatial distribution of the wall-parallel force component f_{x0} determined by the equations (9) is shown on Fig. 2, *a*. Comparison with the distribution of the "seeming" wall-parallel force component f_{x1} reconstructed in experiments by the method 1 and presented in Fig. 8, *a* in [26] demonstrates that the maximal value $f_{x0\max} \approx 8.5$

DOI: 10.13009/EUCASS2017-13

kN/m^3 achieving on the dielectric surface slightly exceeds the experimental value $f_{x1\max} \approx 8$ kN/m^3 which observed above the surface.

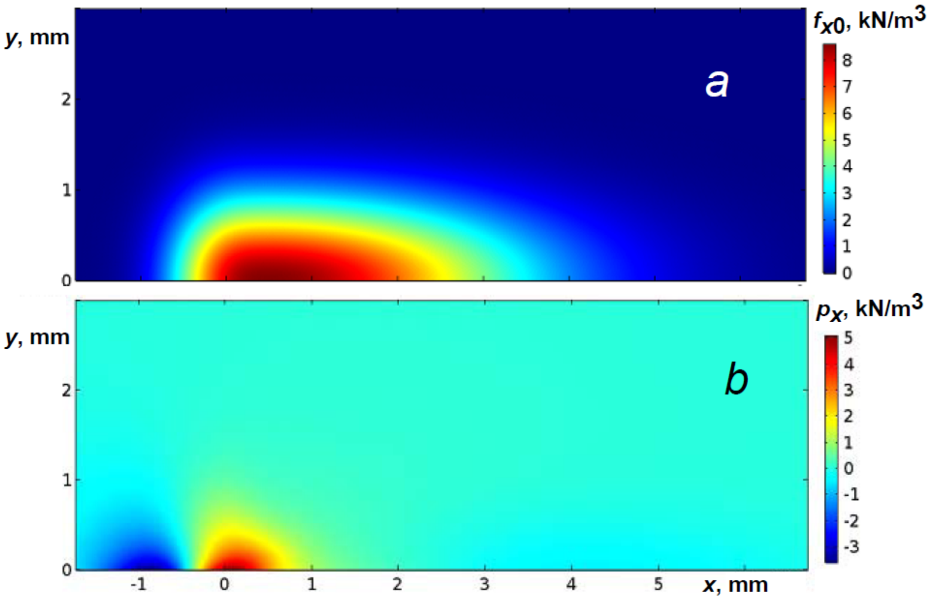

Figure 2: Distributions of the given wall-parallel force (*a*), the induced wall-parallel pressure gradient (*b*)

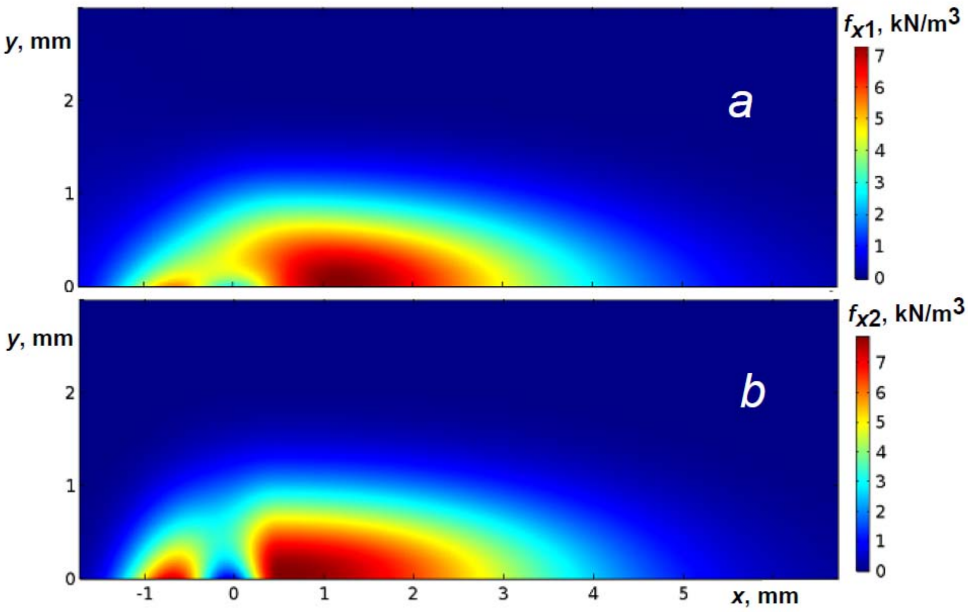

Figure 3: Distributions of the calculated "seeming" wall-parallel force component f_{x1} (*a*), f_{x2} (*b*)

The calculated distribution of the wall-parallel gradient of static pressure $\partial p/\partial x$ induced by actuator action is shown on Fig. 2, *b*. First of all note, that the induced pressure gradient on absolute magnitude is comparable with the wall-parallel force, as it has been shown earlier in [27, 28]. It means that the first assumption (3) in the method 1 is incorrect. The wall-parallel pressure gradient is negative to the left from the exposed electrode edge at $x \leq 0.3$ mm. It seems evident that namely this region of negative pressure gradient propagating far enough upstream (where the volumetric force decays) supports a flow acceleration before the electrode edge. The pressure gradient becomes positive downstream in the region of maximal concentration of the volumetric force and thereby attenuates the force impact of actuator. Further downstream at $x \geq 2.4$ mm a stretched region of low intensive negative pressure gradient appears again in such a way supporting flow acceleration.

Mentioned features of the wall-parallel pressure gradient permit to explain the peculiarities of the "seeming" force component f_{x1} denoted as 1 and 3 in the item 2. The distribution of the residual of the given force and the induced

DOI: 10.13009/EUCASS2017-13

pressure gradient $f_{x1} = fx_0\text{-}\partial p/\partial x$ is shown on Fig. 3, *a*. The upstream region of the negative pressure gradient reveals as local region of elevated force on the left from the electrode edge, in accordance with the peculiarity 1. The region of positive pressure gradient, at first, decreases the maximal value of the "seeming" force f_{x1} and, at second, shifts its maximum from the wall, accordingly the peculiarity 3.

The analytic distribution (9)-(10) permits to calculate an analogue of the "seeming" wall-parallel force component f_{x2} recovered by the method 2. Substitution of $f_x = f_{x0}$ and $f_y = f_{y0}$ in the left side of the equation (6) results in

$$
\begin{aligned}
x \le x_m: \quad & f_{x2}(x,y) = f_{x0} + A\frac{y_0^2}{x_l^2}\left[2a\bar{x}^4 - (5a-2)\bar{x}^2 + a - 1\right]\times \\
& \times \exp\left(-\bar{x}^2\right)\left[\exp\left(-\bar{y}^2\right) - \sqrt{\pi}\,\bar{y}\,\mathrm{erfc}(\bar{y})\right], \\
x > x_m: \quad & f_{x2}(x,y) = f_{x0} + A\frac{y_0^2}{x_r^2}\left(2\bar{x}^2 - 1\right)\times \\
& \times \exp\left(-\bar{x}^2\right)\left[\exp\left(-\bar{y}^2\right) - \sqrt{\pi}\,\bar{y}\,\mathrm{erfc}(\bar{y})\right]
\end{aligned}
\tag{11}
$$

It is evident from (11) that the continuity of the second derivative of f_{x0} on x ensures a continuity of f_{x2} at $\bar{x} = 0$. The distribution (11) is shown on Fig. 3, *b*. This distribution, similar to Fig. 3, *a*, contains the upstream region of elevated force but more intensive than in Fig. 3, *a*. Thus the explanation of the peculiarities 1 and 2 of the item 2 is given.

The identity of the total wall-parallel force recovered by two methods (peculiarity 4) seems to be evident. The conditions of decay of static pressure disturbances caused by actuator action and volumetric force at infinity result in

$$p(-\infty, y) = p(\infty, y) = p_\infty \quad \Rightarrow \int_0^{+\infty} dy \int_{-\infty}^{+\infty} \frac{\partial p}{\partial x}(x,y)dx = \int_0^{+\infty} p(+\infty, y)dy - \int_0^{+\infty} p(-\infty, y)dy = 0.$$

$$f_y(-\infty, y) = f_y(\infty, y) = 0 \quad \Rightarrow \int_0^{+\infty} dy \int_{-\infty}^{+\infty} dx \int_y^{+\infty} \frac{\partial f_y}{\partial x}(x,s)ds = \int_0^{+\infty} dy \int_y^{+\infty} \left[f_y(+\infty, s) - f_y(-\infty, s)\right]ds = 0,$$

Hence the spatial integration of the "seeming" force components determined by the relations (1) and (6) results in the identical values of the total force

$$\int_0^{+\infty} dy \int_{-\infty}^{\infty} f_{x1} dx = \int_0^{+\infty} dy \int_{-\infty}^{\infty} \left(f_x - \frac{\partial p}{\partial x}\right) dx = \int_0^{+\infty} dy \int_{-\infty}^{\infty} f_x dx = F,$$

$$\int_0^{+\infty} dy \int_{-\infty}^{\infty} f_{x2} dx = \int_0^{+\infty} dy \int_{-\infty}^{\infty} \left[f_x + \int_y^{\infty} \frac{\partial f_y}{\partial x}(x,s)ds\right] dx = \int_0^{+\infty} dy \int_{-\infty}^{\infty} f_x dx = F.$$

The volumetric force components determined by the expressions (9)-(10) don't satisfy the simplifying assumption (5) of the method 2. The distribution of the given wall-normal component force f_{y0} is presented on Fig. 4, *a*. First of all note that the maximal value of this component is comparable with a maximum of the wall-parallel force component, in contrast to experimental data concerning "seeming" force recovered by the method 1 and presented on Fig. 8, *a*, *b* in [26]. The wall-normal force component f_{y0} is positive on the left from the point of maximum of the wall-parallel component $x_m = 0.5$ mm and is negative on the right from this point. It means that the vectors of the volumetric force determined by the model (9)-(10) are directed upward and right in the whole semi-space situated at the left from vertical line $x_m = 0.5$ mm. Respectively the force vectors are directed downward and right in semi-space $x > 0.5$ mm. Note that this feature of the volumetric force field agrees with numerical modeling of DBD [13]. At the same time it is very difficult to imagine a behavior of the field lines of the "seeming" force seeing on the distribution of the wall-normal component presented on Fig. 8, *b* in [26] (see also peculiarity 6 in the item 2).

Nevertheless this peculiarity can be explained in the framework of the present model of the volumetric force. The calculated distribution of the induced wall-normal pressure gradient is shown on Fig. 4, *b*. Comparison of Figs. 4, *a* and *b* demonstrates that this pressure gradient almost completely compensates the wall-normal force. The residual of the force and pressure gradient difference $f_{y1} = fy_0\text{-}\partial p/\partial y$ is shown on Fig. 4, *c*. It is seen that the "seeming" wall-normal force f_{y1} is about the order of magnitude less than the wall-parallel force, in accordance with experiments [26]

DOI: 10.13009/EUCASS2017-13

where the wall-normal force component varies in the range from -0.8 up to 0.8 kN/m^3. Moreover, the distribution of f_{y1} shown on Fig. 4, *c* contains the region of sign-alternating force near the electrode edge in conformity with the experimental distribution presented on Fig. 8, *b* in [26]. Thus the peculiarities 5 and 6 are explained too.

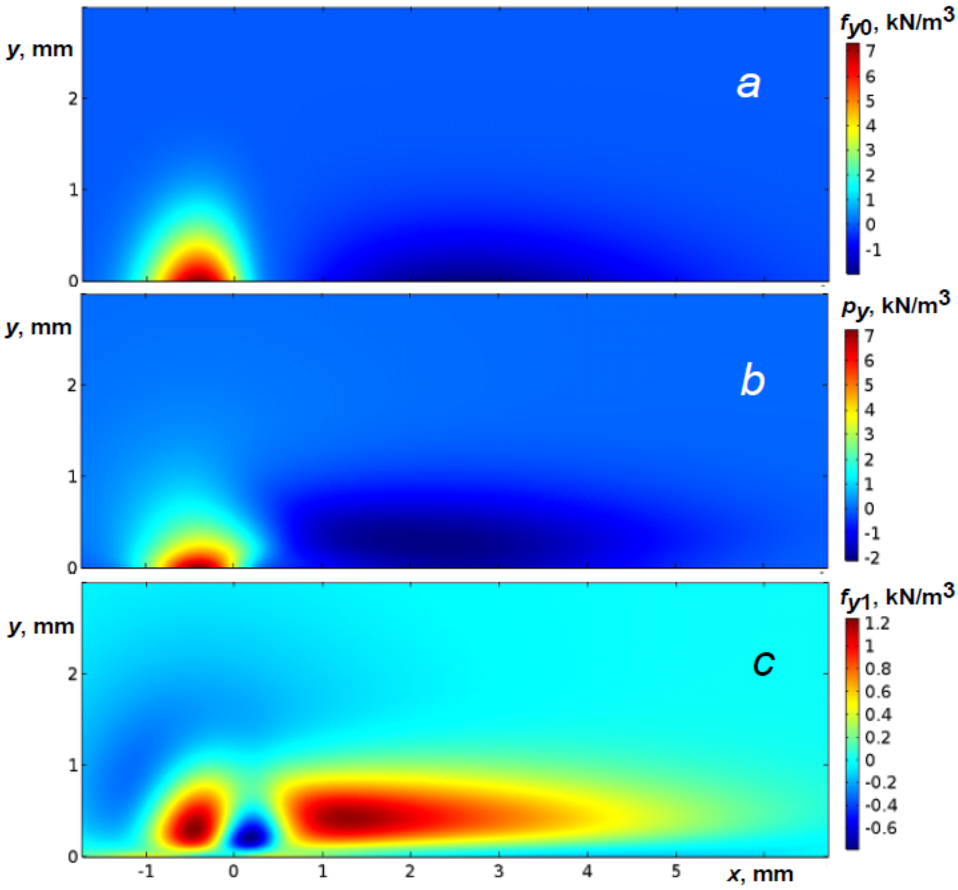

Figure 4: Distributions of the given wall-normal force component f_{x0} (*a*), the induced wall-normal pressure gradient (*b*), the calculated "seeming" wall-normal force component f_{y1} (*c*)

A presence of experimentally observed near-wall region of intense negative wall-parallel force arising at some distance from the exposed electrode and propagating downstream (see Fig. 8, *a* in [26]) can not be explained in the framework of DBD physics. By our opinion, this phenomenon is related with turbulent stresses developing in near-wall jet. Thorough numerical modeling of the considered flow induced by DBD-actuator executed in [19] on the basis of Steady Reynolds-Averaged Navier-Stokes (RANS) equations revealed the transient character of jet flow closer to turbulent case. Executed in [19] analysis of experimental and calculated velocity distributions with taking into account theoretical consideration of near-wall jet stability [32] confirmed this conclusion. The necessity to use RANS equation in force-determination methods is emphasized also in [33].

The analysis of the hydrodynamic stability of the jet flow presented on Fig. 1 fulfilled in the framework of well-known eigenvalue problem for Orr-Sommerfeld equation gives other confirmation of transient character of the considered flow. Unsteady disturbances of velocity components and pressure have been specified in the form $q(x,y,t) = q^*(y)\exp[i(\alpha x - \omega t)]$, $\alpha = \alpha_r + i\alpha_i$, $\omega = 2\pi f$, where q^* is the complex eigenfunction, α is the complex wave number, ω is the real circular frequency. The calculated neutral stability curve and velocity profiles in some cross-sections with the velocity scale above the first velocity profile are shown on Fig. 5, *a*. The increments of spatial growth of disturbances $a = -\alpha_i$ are presented on Fig. 5, *b*. It is evident that the considered flow is highly unstable.

In the case of turbulent flow the application of the force-determination method 1 results in the following equation for the "seeming" wall-parallel force component:

$$f_{x1T}(x,y) \equiv f_x - \frac{\partial p}{\partial x} + \mu_T\left(\frac{\partial^2 u}{\partial x^2} + \frac{\partial^2 u}{\partial y^2}\right) = \rho\left(u\frac{\partial u}{\partial x} + v\frac{\partial u}{\partial y}\right) - \mu\left(\frac{\partial^2 u}{\partial x^2} + \frac{\partial^2 u}{\partial y^2}\right). \tag{12}$$

DOI: 10.13009/EUCASS2017-13

Here μ_T is the eddy viscosity and, again, only terms in right side of this equation is known from measurements of the velocity field. The “seeming” wall-parallel force component includes in this case both unknown pressure gradient and Reynolds stress term. By our opinion, the last reveals as near-wall region of negative wall-parallel force in experimental distributions. To verify this assumption, the calculation of RANS has been executed with the use of standard k-ε model [34] for termination of eddy viscosity. The results of calculation presented below are only demonstrational, taking into account many limitations of the used model of turbulence.

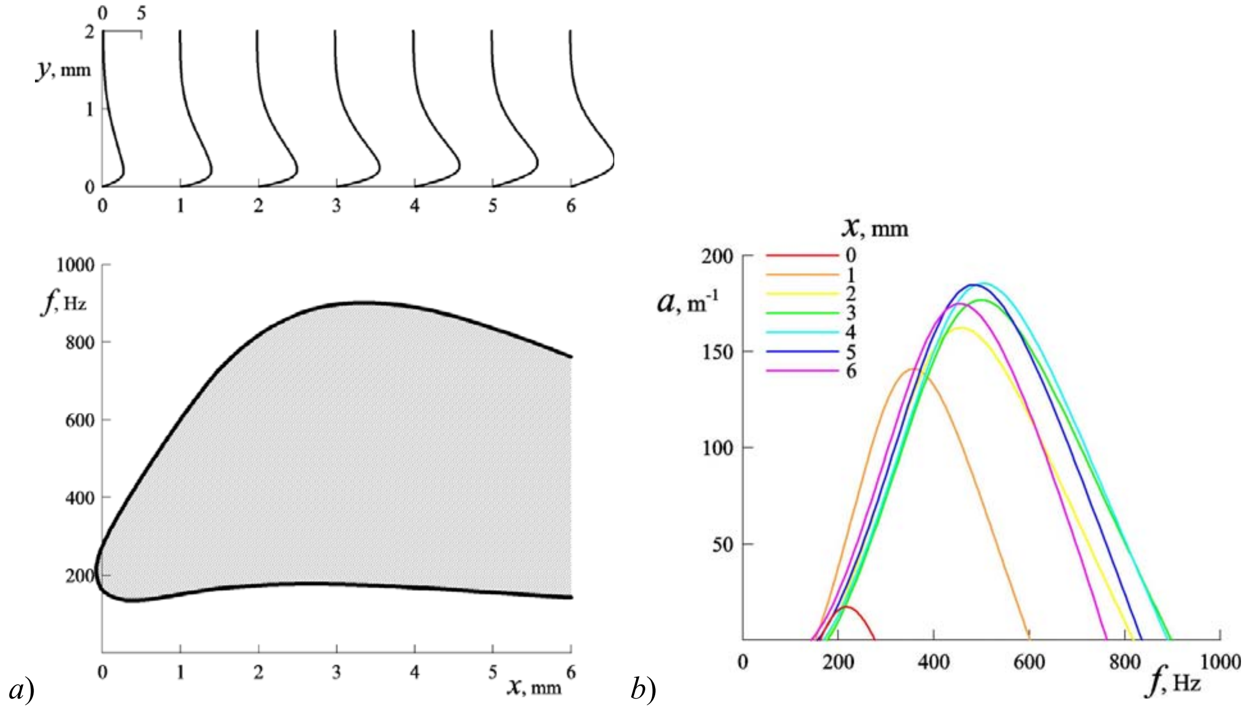

Figure 5: Jet flow velocity profiles and neutral stability curve (a), increments of spatial growth of unsteady disturbances (b)

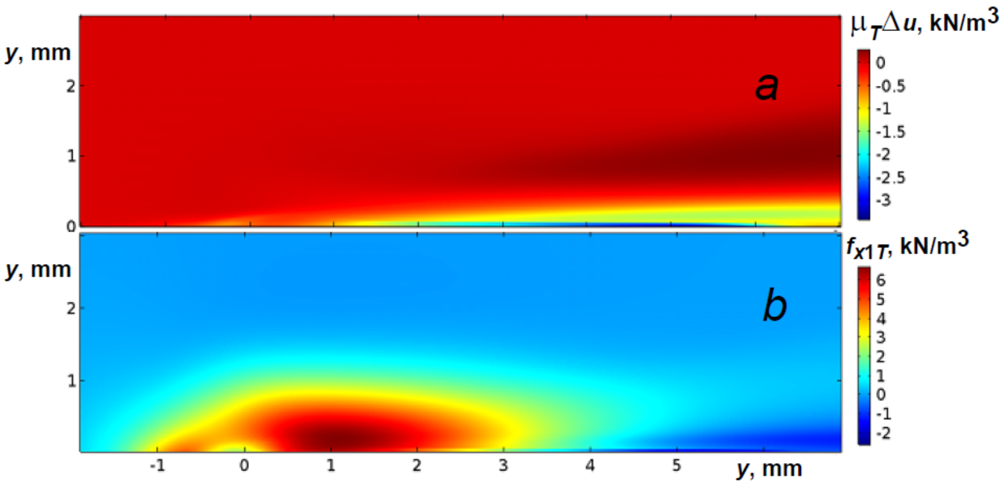

Figure 6: Distributions of the Reynolds stress term (a), the “seeming” wall-parallel force component f_{x1T} (b)

The distribution of the calculated Reynolds stress term is shown on Fig. 6, a. The region of intense turbulent dissipation begins at $x \approx 1$ mm and propagates expanding downstream. The distribution of the resultant “seeming” wall-parallel force f_{x1T} shown on Fig. 6, b is in good qualitative agreement with the experimental distribution on Fig. 8, a in [26]. Note that the minimal negative value of this component obtained in our modelling coincides with the experimental one. So the last peculiarity 7 in the item 2 seems to be explained.

DOI: 10.13009/EUCASS2017-13

5. Conclusion

The nondivergent field approximation for the time-averaged volumetric force generated by DBD-actuator permits to explain main peculiarities of distributions of the volumetric force components obtained by two well-known differential force-determination .methods based on PIV-measurements of velocity fields. It is established that main simplifying assumptions used in both methods are unjustified. Absolute values of the components of both body force and pressure gradient in actuator induced jet flow are comparable. Namely taking into account the induced pressure gradient explains the most of peculiarities of the experimental force distributions. Seeming occurrence of intense negative wall-parallel force arising downstream from the exposed electrode apparently is explained by a neglect of Reynolds stresses developing in unstable jet flow. The proposed simple analytic expressions for the volumetric force components seem to be an adequate model for time-averaged volumetric force generated by DBD-actuator.

References

[1] Moreau, E. Airflow control by non-thermal plasma actuators. 2007. *J. Phys. D: Appl. Phys.* 40: 605-636.

[2] Corke, T.C., M.L. Post, and D.M. Orlov. 2007. SDBD plasma enhanced aerodynamics: concepts, optimization and applications. *Progr. Aerospace Sci.* 43: 193-217.

[3] Corke, T.C., C.L. Enloe, and S.P. Wilkinson. 2010. Dielectric barrier discharge plasma actuators for flow control. *Annu. Rev. Fluid Mech.* 42: 505-529.

[4] Wang, J.J., K-S. Choi, L-H. Feng, T.N. Jukes, and R.D. Whalley. 2013. Recent developments in DBD plasma flow control. *Progr. Aerospace Sci.* 62: 52-78.

[5] Benard, N., and E. Moreau. 2014. Electrical and mechanical characteristics of surface AC dielectric barrier discharge plasma actuators applied to airflow control. *Exp. Fluids.* 55: 1846 (43 pp.).

[6] Leonov, S.B., I.V. Adamovich, and V.R. Soloviev. 2016. Dynamics of near-surface electric discharges and mechanisms of their interaction with the airflow. *Plasma Sources Sci. Technol.* 25: 063001 (32 pp).

[7] Kriegseis, J., D. Simon, and S. Grundmann. 2016. Towards in-flight applications? A review on dielectric barrier discharge-based boundary-layer control. *Trans. of the ASME. Appl. Mech. Rev.* 68: 020802 (41 pp).

[8] Thomas, F.O., T.C. Corke, M. Iqbal, A. Kozlov, and D. Schatzman. 2009. Optimization of dielectric barrier discharge plasma actuators for active aerodynamic flow control. *AIAA Journal.* 47(9): 2169–2178.

[9] Boeuf, J.P., Y. Lagmich, T. Unfer, Th. Callegari, and L.C. Pitchford. 2007. Electrohydrodynamic force in dielectric barrier discharge plasma actuators. *J. Phys. D: Appl. Phys.* 40: 652–663.

[10] Singh, K.P., and S. Roy. 2007. Modeling plasma actuators with air chemistry for effective flow control. *J. Appl. Phys.* 101: 123308.

[11] Likhanskii, A.V., M.N. Shneider, S.O. Macheret, and R.B. Miles. 2008. Modeling of dielectric barrier discharge plasma actuator in air. *J. Appl. Phys.* 103: 055505.

[12] Soloviev, V. R., and V. M. Krivtsov. 2009. Surface barrier discharge modelling for aerodynamic applications. *J. Phys. D: Appl. Phys.* 42: 125208 (13 pp).

[13] Kuryachii, A. P., D. A. Rusyanov, S. L. Chernyshev, and V. V. Skvortsov. 2013. About increase of efficiency of plasma multi-actuator system for boundary layer control. *TsAGI Sci. J.* 44(3): 305-326.

[14] Shang, J.S., and P.G. Huang. 2014. Modeling surface plasma actuators for flow control. AIAA Paper 2014-0324 (23 pp).

[15] Shyy,W., B. Jayaraman, and A. Andersson. 2002. Modeling of glow discharge-induced fluid dynamics. *J. Appl. Phys.* 92 (11): 6434-6443.

[16] Suzen, Y. B., P. G. Huang, J. D. Jacob, and D. E. Ashpis. 2005. Numerical simulations of plasma based flow control applications. AIAA Paper 2005-4633 (11 pp).

[17] Mertz, B.E. and T.C. Corke. 2011. Single-dielectric barrier discharge plasma actuator modelling and validation. *J. Fluid Mech.* 669: 557–583.

[18] Kuryachii, A. P., S.V. Manuilovich, D. A. Rusyanov, V. V. Skvortsov, and S. L. Chernyshev. 2014. On the possibility of laminar flow control on a swept wing by means of plasma actuators. *TsAGI Sci. Journal.* 45(6): 531–554.

[19] Maden, I., R. Maduta, J. Kriegseis, S. Jakirlić, C. Schwarz, S. Grundmann, and C. Tropea. 2013. Experimental and computational study of the flow induced by a plasma actuator. *Int. J. Heat Fluid Flow*. 41: 80–89.

[20] Dörr, P. C., and M. J. Kloker. 2015. Numerical investigation of plasma actuator force-term estimations from flow experiments. *J. Phys. D: Appl. Phys.* 48: 395203 (16 pp).

[21] Ustinov, M.V. 2016. Numerical modeling of the laminar-turbulent transition control using a dielectric barrier discharge. Fluid Dynamics. 51(2): 200–213.

[22] Benard, N., M. Caron, and E. Moreau. 2015. Evaluation of the time-resolved EHD force produced by a plasma actuator by particle image velocimetry – a parametric study. *J. Phys.: Conference Series* 646: 012055 (5 pp).

DOI: 10.13009/EUCASS2017-13

[23] Wilke, B. 2009. Aerodynamische Strömungssteuerung mittels dielektrischen Barriereentladungs-Plasmaaktuatoren. Ph.D. thesis, Technische Universität Darmstadt, DLR Göttingen.
[24] Albrecht, T., T. Weier, G. Gerbeth, H. Metzkes, and J. Stiller. 2011. A method to estimate the planar, instantaneous body force distribution from velocity field measurements. *Phys. Fluids.* 23: 021702 (4 pp).
[25] Kriegseis, J., C. Schwarz, A. Duchmann, S. Grundmann, and C. Tropea. 2012. PIV-based estimation of DBD plasma-actuator force terms. AIAA Paper 2012-0411 (12 pp).
[26] Kriegseis, J., C. Schwarz, C. Tropea, and S. Grundmann. 2013. Velocity-information-based force-term estimation of dielectric-barrier discharge plasma actuators. *J. Phys. D: Appl. Phys.* 46: 055202 (13 pp).
[27] Kuryachii, A. P., S.V. Manuilovich, and D. A. Rusyanov. 2016. Approximation of distributions of the volumetric force generated by a plasma actuator. *TsAGI Sci. Journal*. 47(5): 495-512.
[28] Manuilovich, S.V. 2016. Role of the pressure gradient in flows controlled by a near-wall body force. *Fluid Dynamics.* 51(4): 482–490.
[29] Manuilovich, S.V. 2015. Longitudinally periodic viscous flows generated by a near-wall volume force. *Fluid Dynamics.* 50(4): 514–521.
[30] Boeuf, J.P., Y. Lagmich Y., and L.C. Pitchford. 2009. Contribution of positive and negative ions to the electrohydrodynamic force in a dielectric barrier discharge plasma actuator operating in air. *J. Appl. Phys.* 106: 023115 (9 pp).
[31] Soloviev, V.R. 2012. Analytical estimation of the thrust generated by a surface dielectric barrier discharge. *J. Phys. D: Appl. Phys.* 45: 025205 (12 pp).
[32] Chun, D.H., and W.H. Schwarz. 1967. Stability of the plane incompressible viscous wall jet subjected to small disturbances. Phys. Fluids. 10(5): 911-915.
[33] Maden, I., K. Barckmann, J. Kriegseis, S. Jakirlić, C. Tropea, and S. Grundmann. 2014. Evaluating force field induced by a plasma actuator using the Reynolds-Averaged Navier Stokes equation. AIAA Paper 2014-0326 (10 pp).
[34] Launder, B.E., and B.I. Sharma. 1974. Application of the energy dissipation model of turbulence to the calculation of flow near a spinning disk. *Letter in Heat & Mass Transfer*. 1(2): 131-138.